Nanoscale

ROYAL SOCIETY OF CHEMISTRY

PAPER

View Article Online
View Journal | View Issue

Cite this: *Nanoscale*, 2020, **12**, 18278

Covalently functionalized layered MoS_2 supported Pd nanoparticles as highly active oxygen reduction electrocatalysts†

Dimitrios K. Perivoliotis, *[a] Yuta Sato, [b] Kazu Suenaga [b] and Nikos Tagmatarchis *[a]

Molybdenum disulfide nanosheets covalently modified with a 1,2-dithiolane derivative were used as a novel substrate for the immobilization of Pd nanoparticles (Pd_{NPs}) towards the development of a highly efficient hybrid electrocatalyst, namely Pd_{NPs}/f-MoS_2, for the oxygen reduction in an alkaline medium. The newly prepared hybrid material was thoroughly characterized through complementary techniques such as Raman and IR spectroscopy, TGA, HRTEM, STEM/EELS, and EDS. The Pd_{NPs}/f-MoS_2 nanohybrid exhibited excellent performance towards oxygen electroreduction with a positive onset potential of +0.066 V and a half-wave potential of −0.116 V *vs.* Hg/HgO, along with a high current response, which are superior to those of its graphene counterpart and comparable to those of the benchmark Pd/C product. Moreover, Pd_{NPs}/f-MoS_2 was proved to be remarkably stable as chronoamperometric assays showed minimum activity loss among the tested materials, clearly outperforming the commercial catalyst. The excellent performance of Pd_{NPs}/f-MoS_2 is attributable to (i) the high affinity of the catalytic Pd_{NPs} with the f-MoS_2 substrate, (ii) the absence of any capping agent for the stabilization of Pd_{NPs} onto f-MoS_2, and more importantly (iii) the preservation of the integrity of the MoS_2 basal plane during the functionalization process. Lastly, the oxygen reduction on Pd_{NPs}/f-MoS_2 proceeded through the energy efficient four-electron pathway, showing great potential for the use of layered transition metal dichalcogenides in energy conversion applications, comprising fuel cells.

Received 11th June 2020,
Accepted 6th August 2020

DOI: 10.1039/d0nr04446f

rsc.li/nanoscale

Introduction

Tailoring electrocatalysts to accelerate the sluggish kinetics of the oxygen reduction reaction (ORR) still remains a key challenge towards the commercialization of the fuel cell technology.[1] In this regard, supported catalysts for the ORR have drawn much attention, since they offer not only enhanced electrocatalytic activities, but also more importantly improved durability. Notably, the efficient interactions between a nanoparticle catalyst and a support could modify the electronic structure of the catalyst, facilitating the oxygen adsorption and dissolution, while, at the same time, prevent nanoparticles from aggregation, contributing to long term stability.[2]

Graphene, a two-dimensional (2D) sp^2 hybridized carbon allotrope, has been widely used as a supporting material, owing to its high surface area and electrical conductivity as well as good chemical stability.[3] Beyond graphene, layered transition metal dichalcogenides, abbreviated as TMDs, constitute another class of 2D materials that combine the exceptional properties of graphene with remarkable intrinsic electrocatalytic activities toward key electrochemical reactions, originating from a large number of exposed prismatic edges.[4,5] Actually, TMDs are atomically thick nanocrystals with MX_2 stoichiometry, where M refers to a transition metal atom (*e.g.* Mo, W, Ta) and X to a chalcogen atom (S, Se, Te).[6] Among various TMDs, molybdenum disulfide (MoS_2) nanosheets have received special scientific attention as they are readily accessible and chemically stable.[7] Liquid phase exfoliation from the bulk material is the most effective way to obtain high quality layered MoS_2 on a large scale.[8–11] Similar to other TMDs, MoS_2 is characterized by a thickness dependent semiconducting behavior and an indirect-to-direct bandgap transition occurs when its thickness decreases to a single layer.[12] Moreover, the MoS_2 monolayer presents a much lower bandgap (~1.2 eV) than typical semiconducting materials (>3 eV),[13] while its elec-

[a]*Theoretical and Physical Chemistry Institute, National Hellenic Research Foundation, 48 Vassileos Constantinou Avenue, 11635 Athens, Greece. E-mail: tagmatar@eie.gr, dimperiv@eie.gr*
[b]*Nanomaterials Research Institute, National Institute of Advanced Industrial Science and Technology (AIST), Central 5, 1-1-1 Higashi, Tsukuba 305-8565, Japan*
†Electronic supplementary information (ESI) available: Additional characterization & electrochemical data. See DOI: 10.1039/d0nr04446f

tronic structure is closely related to the coordination of the Mo atoms. All in all, these fascinating properties give layered MoS_2 a clear advantage over graphene, making it an attractive component for potential use in energy conversion (electrocatalysis[14] and (photo)-electrocatalysis[15]) and storage[16–19] applications.

Similar to graphene, in order to fully exploit the intriguing properties of layered TMDs, their chemical functionalization is an absolute necessity.[20] Needless to mention, the introduction of functional groups on their surface could not only solve the problem of their limited solubility in common solvents and restacking of nanosheets, but also allows the design of entirely new hybrid materials. Markedly, the covalent attachment of the appropriate organic moieties on MoS_2 sheets' surface makes them ideal platforms for the immobilization of various catalytic nanoparticles by effectively tuning the interfacial interactions and thereby leading to the formation of hybrids with increased electrocatalytic activity and excellent durability. To date, diverse methodologies have been developed towards the covalent functionalization of layered MoS_2,[21] including the reaction with electrophiles *e.g.* organoiodides and aryldiazonium salts[22] and organic thiols.[23] In the latter case, a Mo–S bond is formed between an unsaturated molybdenum atom in MoS_2 and a sulfur atom in the organic functional group. Interestingly, unsaturated Mo atoms are dominant at the edges of the MoS_2 nanosheets, where structural defects (S vacancies) have been naturally introduced during the exfoliation process.[8] Therefore, the MoS_2 basal plane remains intact and hence its exceptional properties, which are essential when considering the design of high performance electrocatalysts, are preserved. However, a major drawback of this approach is related to the possible conversion of thiols into the corresponding disulfides – a reaction that is activated in the presence of MoS_2. Based on this, an alternative route employing 1,2-dithiolanes as robust thiol groups to react with exfoliated MoS_2 sheets has been recently developed.[24]

Despite the huge potential of MoS_2 as a catalyst substrate, only a few reports have been published employing MoS_2 sheets as a supporting material for metal-based catalytic nanoparticles towards the ORR.[25–27] Actually, the main bottlenecks that keep MoS_2 behind the scenes are related to their low conductivity and the poor dispersity and the homogeneity of the resulting hybrids.[14] Therefore, developing efficient synergistic interactions between MoS_2 sheets and noble metal nanoparticles is essential to overcome these limitations.[28] To this end, diverse methodologies[25,26] *e.g.* epitaxial growth, physical mixing, and sonochemical approaches, have been involved for the preparation of such hybrid materials aiming at the optimization of the ORR performance of the supported catalysts. Despite the advancements that have been made in the field, the ORR performance of the reported hybrids still needs improvement to compete with the benchmark catalysts. In the same context, the surface functionalization of MoS_2 sheets could tune the intra-hybrid interactions, and hence significantly boost the performance of the hybrid electrocatalysts. However, to the best of our knowledge, the use of modified layered MoS_2 as an ORR catalyst substrate has not been reported yet.

The present work goes beyond the current state-of-the-art by employing covalent functionalized MoS_2 nanosheets with a 1,2-dithiolane derivative (f-MoS_2), featuring free amino groups, as a substrate for immobilization of Pd nanoparticles (Pd_{NPs}). The obtained hybrid, abbreviated as Pd_{NPs}/f-MoS_2, was examined as the electrocatalyst for the ORR under alkaline conditions and its performance was further compared with that of its counterpart based on functionalized graphene (f-G), abbreviated as Pd_{NPs}/f-G. The results clearly demonstrated an overall improved performance of Pd_{NPs}/f-MoS_2 over that of Pd_{NPs}/f-G, highlighting the benefits of using the TMD-based substrate. The exceptional ORR activity and stability of Pd_{NPs}/f-MoS_2 was ascribed to (i) the high affinity of Pd_{NPs} with the f-MoS_2 substrate, (ii) the absence of any capping agent for the stabilization of Pd_{NPs} onto f-MoS_2 and more importantly (iii) the preservation of the integrity of the MoS_2 basal plane during the functionalization process. Markedly, the latter explains to a large extent why Pd_{NPs}/f-MoS_2 outperforms the graphene-based Pd_{NPs}/f-G electrocatalyst as in this case the covalent functionalization induces damage to the graphene lattice leading to the deterioration of its inherent properties. Generally speaking, the latter is the main obstacle in using covalently functionalized graphene as a component in electrocatalytic applications and thus the current research on graphene-based electrocatalysts has been focused on non-covalently modified as well as doped graphene.[3,29–31] This work proposes the use of covalently edge-functionalized MoS_2 nanosheets as platforms for the fabrication of the next generation of hybrid electrocatalysts, paving the way for their further use in real energy conversion applications.

Results and discussion

Preparation

The preparation of Pd_{NPs}/f-MoS_2 and Pd_{NPs}/f-G hybrids is illustrated in Scheme 1. First, MoS_2 and graphene sheets were covalently functionalized with organic moieties bearing free amino groups to enable the attachment of Pd_{NPs} on their surface. As for MoS_2, exfoliated MoS_2 nanosheets (exf-MoS_2) were obtained upon chlorosulfonic acid treatment of the bulk material[8] and modified with the 1,2-dithiolane *N-tert*-butoxycarbonyl (BOC) derivative. Notably, the latter reaction is based on the high binding affinity of the 1,2-dithiolane component for the Mo atoms that are located at the edges of MoS_2, where sulfur vacancy sites were introduced during the exfoliation process.[24] On the other hand, graphite was oxidized to graphene oxide (GO) and the GO functionalization was realized upon (i) activation of the carboxylic acid groups by acyl chloride followed by the condensation reaction with BOC-2,2′-(ethylenedioxy)bis-ethylamine[32] and (ii) the ring-opening reaction of the epoxy groups present on the graphene lattice by the nucleophilic attack of the BOC-2,2′-(ethylenedioxy)bis-ethylamine, yielding covalently functionalized graphene sheets at

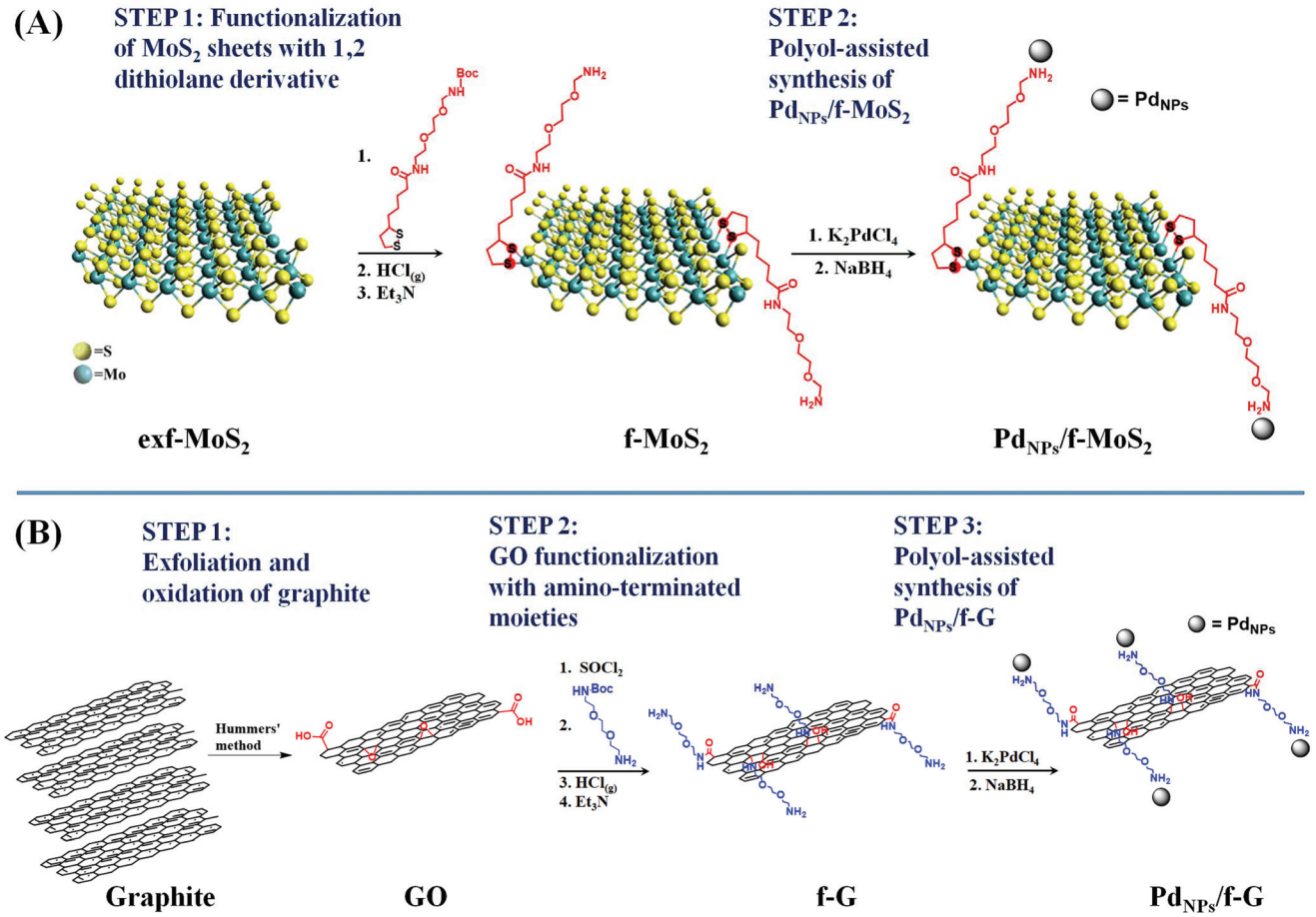

Scheme 1 Illustrative scheme for the preparation protocol of (A) Pd_{NPs}/f-MoS_2 and (B) Pd_{NPs}/f-G hybrids.

both edges and the basal plane simultaneously.[33] Importantly, in both MoS_2 and graphene modified nanosheets, the attached amine species were masked with the BOC-protecting group, which was effectively cleaved after acidic treatment, yielding amino functionalized MoS_2 and graphene materials, respectively (Scheme 1). Afterwards, a modified polyol method was employed for the *in situ* synthesis and immobilization of Pd_{NPs} onto f-MoS_2 and f-G substrates towards the realization of Pd_{NPs}/f-MoS_2 and Pd_{NPs}/f-G hybrids. At this point, it is worth noting that the free amino groups serve as anchoring sites for metal-ion nucleation and subsequent nanoparticle growth, stabilizing effectively the *in situ* formed nanoparticles without using any additional capping agent, which significantly impair their electrocatalytic activity.[34,35]

Characterization

Direct proof for the formation of f-MoS_2 was given by complementary characterization tools. In this context, the ATR-IR spectrum of BOC-modified MoS_2 is governed by bands in the 2840–2960 cm^{-1} range owing to the alkyl chain C–H vibration modes, while two discrete bands at 1645 and 1707 cm^{-1} attributed to carbonyl amide and BOC units, respectively, are also present (Fig. 1, panel A). Interestingly, the band of the latter is absent in the ATR-IR spectrum of f-MoS_2, indicating the successful BOC deprotection process. Moreover, a band at 3225 cm^{-1} owing to the N–H stretching can be observed in the ATR-IR spectrum of f-MoS_2, further proving the presence of the free amine group on the MoS_2 surface. Next, Raman analysis of f-MoS_2 and exf-MoS_2 sheets further confirmed the accomplishment of MoS_2 covalent functionalization (Fig. 1, panel B). Upon excitation at 633 nm, which produces resonance Raman enhancement of the first and second order vibrational modes, both exf-MoS_2 and f-MoS_2 Raman spectra clearly revealed four dominant Raman bands, namely A_{1g}-LA(M), $E^1{}_{2g}$, A_{1g} and 2LA (M) at 177, 378, 405 and 450 cm^{-1}, respectively. The $E^1{}_{2g}$ and A_{1g} modes derive from the in-plane and out-of-plane vibrations within the S–Mo–S layer, while the 2LA(M) vibration mode is closely related to the S vacancies.[36,37] Therefore, the intensity ratio of 2LA(M) to A_{1g} is commonly used as an indicator to quantify the functionalization degree in layered MoS_2 materials.[38–40] Here, the 2LA(M)/A_{1g} value was found to be decreased for f-MoS_2, implying the elimination of S vacancies due to the functionalization process. The latter observation was further confirmed through complementary Raman mapping assays, revealing an average intensity ratio 2LA(M)/A_{1g} of 0.75 for f-MoS_2 *versus* 1.35 for the exfoliated MoS_2

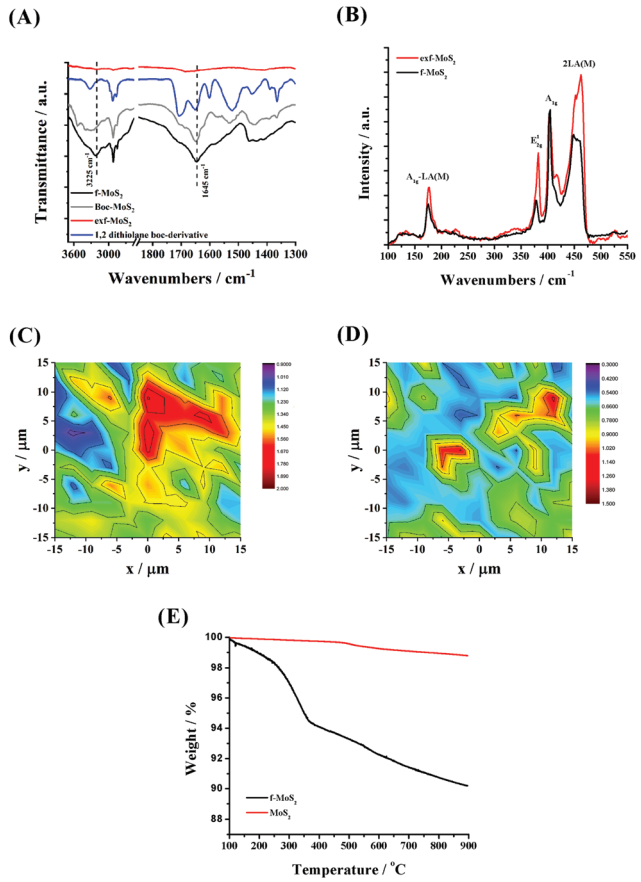

Fig. 1 (A) ATR-IR spectra for amino functionalized MoS_2 (black), BOC modified MoS_2 (gray) and 1,2-dithiolane derivatives (blue). (B) Raman spectra for amino functionalized MoS_2 (black) and exfoliated MoS_2 (red) upon excitation at 633 nm. (C and D) Raman mapping upon excitation at 633 nm of the 2LA(M)/A_{1g} intensity ratio of a 30 × 30 mm^2 area (121 acquisition points in total) for exf-MoS_2 and f-MoS_2, respectively. (E) Thermographs for amino functionalized MoS_2 (black) and exfoliated MoS_2 (red).

sheets, as presented in panels C and D of Fig. 1. Please note that we have performed various mappings in both exf-MoS_2 and f-MoS_2 materials (5 mappings with 121 acquisition points each) and we here present a representative one close to the total average. It is also worth mentioning that no significant changes in the f-MoS_2 Raman spectrum are observed after the immobilization of Pd_{NPs}, suggesting that no structural alterations occurred during the synthesis of the hybrid material (Fig. S1†). Lastly, the functionalization degree was quantified by means of thermogravimetric analysis (TGA). Given that exf-MoS_2 sheets are thermally stable up to 900 °C, the weight loss (around 6%) observed in the temperature range 200–500 °C for f-MoS_2 (Fig. 1, panel E) is ascribed to the thermal decomposition of the covalently grafted organic functionalities onto f-MoS_2. Based on these data, the loading of the organic material was calculated to be 186 µmol g^{-1}.

Concerning f-G, ATR-IR assays provided spectroscopic proof for the success of the functionalization (Fig. S2,† panel A). In short, although the IR spectrum of GO is governed by bands centered at 1720 cm^{-1} (carbonyl C=O), the BOC-functionalized graphene material manifests a different and broad band at 1708 cm^{-1} due to the BOC protecting groups and the carbonyl amide formed. Moreover, strong vibration bands are recorded in the region 2840–2960 cm^{-1} (C–H stretching and bending) and at 3225 cm^{-1} (N–H stretching), further proving the attachment of the organic moiety onto graphene nanosheets. Notably, in the IR spectrum of f-G, in which free amine functionalities are present, the band related to the BOC unit was disappeared, while a pronounced peak at 1655 cm^{-1} derived from the carbonyl amide is present. The epoxy group ring-opening reaction is also confirmed *via* ATR-IR measurements, as the bands assigned to the C–O–C vibrations (at 1200–1250 cm^{-1}) that are observed in the GO spectrum are absent in both BOC-G and f-G materials. Raman spectroscopy was employed to estimate the disorder degree in f-G (Fig. S2,† panels B–D) through the evaluation of the relative intensity of the defect activated D-band at around 1350 cm^{-1}.[41] Briefly, the D/G intensity ratio for f-G was found to be close to 1.0, witnessing its defective nature. Notably, the presence of sp^3 hybridized carbon atoms is mainly related to the introduction of the oxygen containing groups (the D/G intensity ratio for GO is around to 0.90) which are essential for further graphene functionalization. It was also demonstrated (Fig. S3†) that the *in situ* synthesis and immobilization of Pd_{NPs} were not affected by the graphene structure. Lastly, the loading of the organic functionalities was determined through TGA (Fig. S2,† panel E) and it was found to be 840 µmol g^{-1}, being considerably higher than that registered for the f-MoS_2 material; in contrast to MoS_2, the GO functionalization takes place at both edges and the basal plane.

The surface morphology of Pd_{NPs}/f-MoS_2 and Pd_{NPs}/f-G hybrids was thoroughly investigated *via* high-resolution and annular dark-field scanning transmission electron microscopy (HRTEM and ADF-STEM, respectively), whereas their elemental composition was probed by energy dispersive spectroscopy (EDS) and electron energy loss spectroscopy (EELS) chemical mapping. The HRTEM images of Pd_{NPs}/f-MoS_2 and Pd_{NPs}/f-G ensembles (Fig. 2, panels A and D) revealed the uniform distribution of Pd_{NPs} onto f-MoS_2 and f-G, respectively, as only a few agglomerations are observed. Actually, the free amino groups possess high affinity with Pd_{NPs}, stabilizing them effectively on f-MoS_2 and f-G substrates.[34] Interestingly, focusing on the Pd_{NPs}/f-MoS_2 HRTEM image, the presence of a few overlapping MoS_2 monolayers is observed, while Pd_{NPs} is mainly located at the edges, in contrast to the case of Pd_{NPs}/f-G hybrids in which Pd_{NPs} can be found on the entire f-G surface. This finding is in good agreement with the hypothesis that the covalent modification of MoS_2 sheets with 1,2-dithiolane derivatives takes place only at their edges. Next, higher magnification ADF-STEM images revealed that the average size of Pd_{NPS} is 2–3 nm for both hybrid materials (Fig. 2, panels B and E), while at the same time, EDS and EELS elemental analysis (Fig. 2, panels C and F) confirmed the existence of Mo, S and Pd for Pd_{NPs}/f-MoS_2 as well as the presence of C and Pd for the Pd_{NPs}/f-G hybrid.

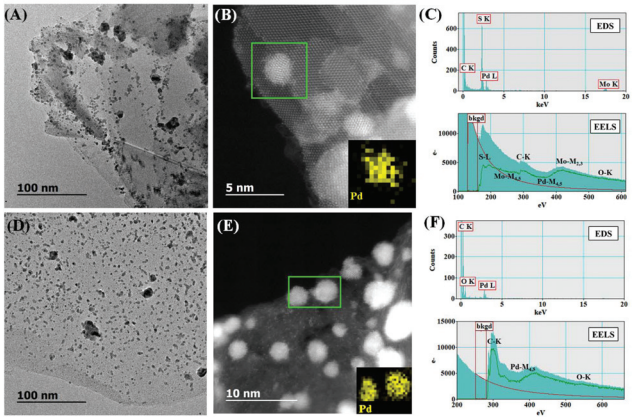

Fig. 2 (A–C) Representative HRTEM and ADF-STEM image along with EELS chemical mapping for Pd and EDS and EELS spectra for Pd_{NPs}/f-MoS_2. (D–F) Representative HRTEM and ADF-STEM image along with EELS chemical mapping for Pd and EDS and EELS spectra for Pd_{NPs}/f-G.

Electrocatalytic performance toward the ORR

To explore the ORR performance of Pd_{NPs}/f-MoS_2 and Pd_{NPs}/f-G electrocatalysts, linear sweep voltammetry (LSV) measurements on the rotating ring-disk electrode (RRDE) were carried out in O_2-saturated 0.1 M KOH electrolyte at a rotation rate of 1600 rpm. As a control, the performance towards the ORR of the benchmark Pd/C catalyst was also recorded. As can be seen in Fig. 3, the Pd_{NPs}/f-MoS_2 hybrid presented by far improved the ORR activity, clearly outperforming its counterpart based on graphene. Indeed, the ORR onset and half-wave potential values of Pd_{NPs}/f-MoS_2 were determined to be +66 and −116 mV (*vs.* Hg/HgO), respectively, being more positive by 50 mV when compared with those recorded for the Pd_{NPs}/f-G hybrid. In addition, the diffusion-limited current density (j_d) for Pd_{NPs}/f-MoS_2 reached 5.70 mA cm^{-2}, whereas its kinetic current density (j_k) was found to be 2.65 mA cm^{-2} at −60 mV (*vs.* Hg/HgO). Notably, these values are 46% and 4.5 times

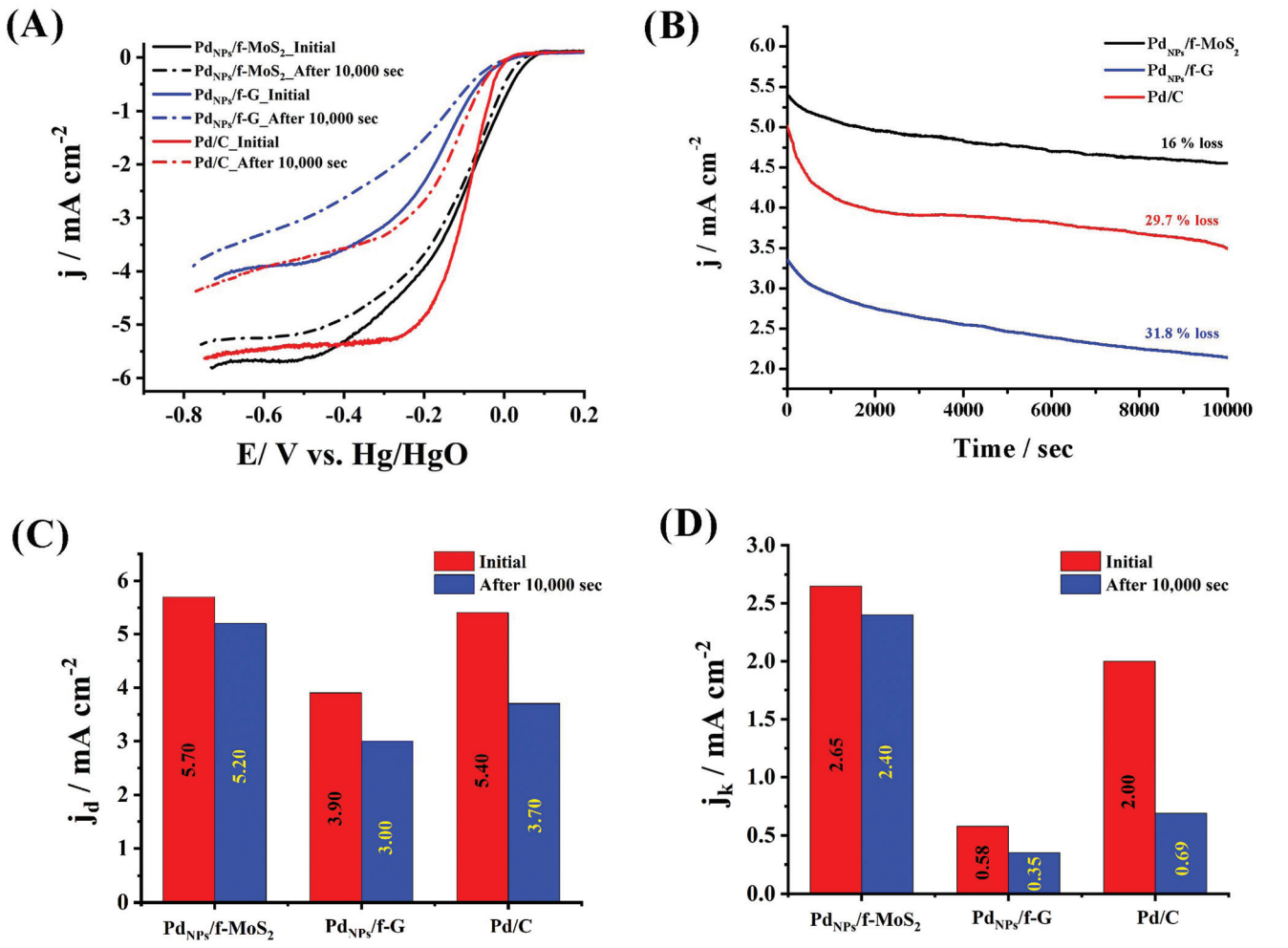

Fig. 3 (A) LSV ORR polarization curves obtained at a rotation speed of 1600 rpm for Pd_{NPs}/f-MoS_2 and Pd_{NPs}/f-G before and after 10 000 s of chronoamperometric assays as compared to that due to Pd/C; (B) ORR chronoamperometric response for all materials at −0.45 V (*vs.* Hg/HgO) for 10 000 s and (C and D) corresponding diffusion limited and kinetic current density values. All measurements were conducted in O_2-saturated 0.1 M KOH electrolyte, and the corresponding electrocatalyst LSVs were recorded at a scan rate of 5 mV s^{-1}. In all graphs, the current densities are normalized to the geometric electrode area.

higher over those of Pd_{NPs}/f-G. Next, the ORR activity of Pd_{NPs}/f-MoS_2 was further compared with that of the state-of-the-art catalyst, showing analogous or enhanced performance, especially in terms of onset potential and kinetic current density. Needless to mention, Pd_{NPs}/f-MoS_2 manifested a more positive onset potential by 53 mV along with a 32.5% greater kinetic current density value at −60 mV (*vs.* Hg/HgO). Overall, the ORR performance of the tested catalysts was in the order of Pd_{NPs}/f-MoS_2 > Pd/C > Pd_{NPs}/f-G. Interestingly, a consistent result was also obtained through durability experiments, in which the chronoamperometric assays of Pd_{NPs}/f-MoS_2, Pd_{NPs}/f-G and Pd/C were performed at a constant applied potential of −0.45 V (*vs.* Hg/HgO) for 10 000 s and a rotation speed of 1600 rpm. As shown in panel B of Fig. 3, the current response of Pd_{NPs}/f-MoS_2 retained 84% of its initial value, whereas an activity loss of 31.8 and 29.7 was recorded for Pd_{NPs}/f-G and Pd/C, respectively. Next, the LSV profiles for all the tested materials after 10 000 s of chronoamperometric assays were recorded in O_2-saturated 0.1 M KOH electrolyte at a rotation rate of 1600 rpm (panel A of Fig. 3). The results clearly demonstrate that the Pd_{NPs}/f-MoS_2 electrocatalyst is remarkably stable, being in total agreement with the chronoamperometric experiments. Needless to say, after 10 000 s, Pd_{NPs}/f-MoS_2 presented less than 10% decrease in its initial diffusion-limited and kinetic current density values, while its half-wave potential value remained almost unchanged. On the other hand, the Pd_{NPs}/f-G material experienced a significant loss of its initial performance (23 and 40% decrease in diffusion-limited and kinetic current density values, respectively, as well as a 26 mV negative shift in the half-wave potential value). Last but not least, after 10 000 s, the MoS_2 based electrocatalyst continues to outperform the commercial Pd/C catalyst by manifesting almost 1.5 and 3.5 times greater diffusion-limited and kinetic current density values, respectively. Interestingly, the observed activity loss after the chronoamperometric assays is mainly attributable to the reduction of the electrochemical active surface area (EASA) of each hybrid electrocatalyst owing to the possible agglomeration of the metal nanoparticles during the chronoamperometric experiment. Given the fact that the EASA is closely related to capacitance,[42–44] the capacitance values for Pd_{NPs}/f-MoS_2 and Pd_{NPs}/f-G hybrids as well as the Pd/C were calculated by integrating the graph area derived from cyclic voltammographs obtained in the "double layer region", according to eqn (6), before and after the chronoamperometric assays.[42] Particularly, it was found that the capacitance value of Pd_{NPs}/f-MoS_2 decreased only by 13.8%, while the same value for Pd_{NPs}/f-G and Pd/C was 43 and 31.5%, respectively (Fig. S4†). Based on these data, the superior stability of Pd_{NPs}/f-MoS_2 is well justified, as it presents the minimum EASA loss, implying the minimum agglomeration.

To elucidate the reaction kinetics, hydrodynamic voltammetry experiments were conducted by altering the electrode's rotation speed. The related ORR polarization curves for Pd_{NPs}/f-MoS_2 and Pd_{NPs}/f-G obtained at different rotation rates between 400 and 3600 rpm are presented in panel A of Fig. 4 and panel A of Fig. S5,† respectively, showing the typical

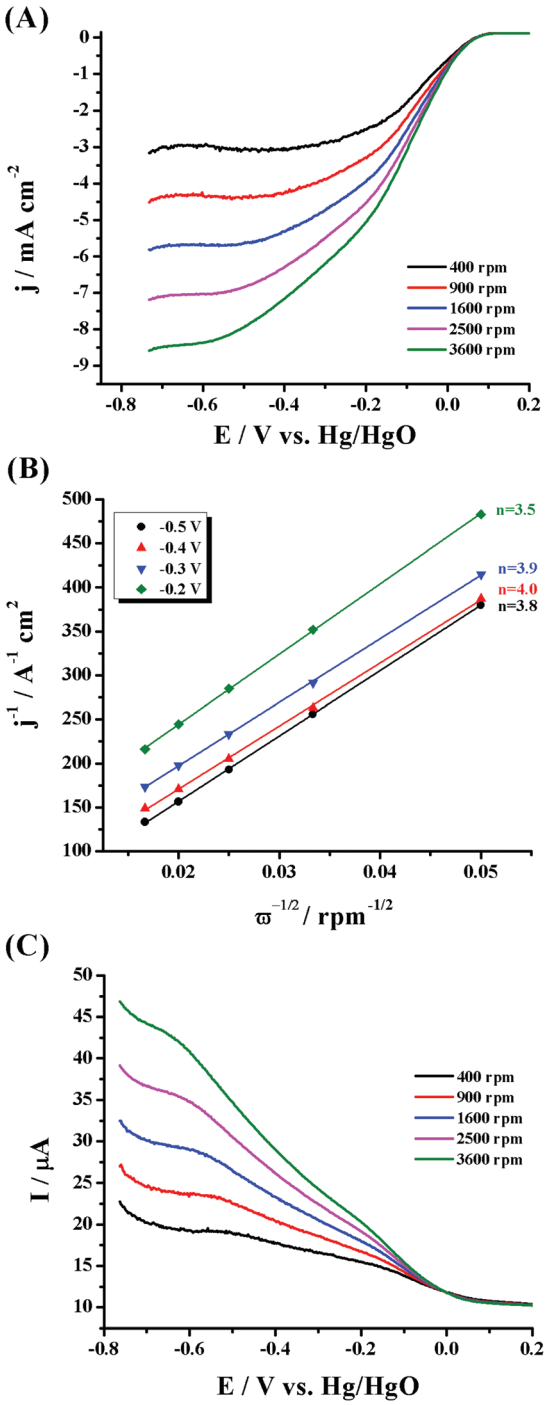

Fig. 4 (A) ORR polarization curves at different rotation rates (400–3600 rpm) for Pd_{NPs}/f-MoS_2, (B) the corresponding K–L plots, and (C) ring response. All measurements were conducted in O_2-saturated aqueous 0.1 M KOH electrolyte, and the corresponding LSV polarization curves were recorded at a scan rate of 5 mV s^{-1}. The ring potential was fixed at 1.0 V *vs.* Hg/HgO. The current densities in (A) are normalized to the geometric electrode area.

increase in current with the increase of the rotation speed due to the shortening of the diffusion layer at high speeds. Next, the corresponding Koutecký–Levich (K–L) plots (Fig. 4, panel B

and Fig. S5,† panel B) were constructed at different potentials based on the inverse of the current density (j^{-1}) against the inverse of the square root of the rotation rate ($\omega^{-1/2}$). As can be seen, these plots presented good linearity, implying first order reaction kinetics towards the dissolved O_2 concentration. Based on these analyses, the electron transfer number per oxygen molecule (n) was estimated and it was found to be 3.6–4.0 and 3.4–3.6 for Pd_{NPs}/f-MoS_2 and Pd_{NPs}/f-G, respectively. Such an n value clearly suggests a four electron selectivity for the MoS_2 based ensemble, in which oxygen reduced directly into water. Lastly, for comparison reasons, the electrocatalytic properties of the f-MoS_2 substrate have also been investigated (Fig. S6†). Briefly, f-MoS_2 was found to present a substantial intrinsic oxygen reduction activity, mainly proceeding through the two-electron pathway (n = 2.1–2.3).

The RRDE approach was applied to further scrutinize the ORR kinetics of Pd_{NPs}/f-MoS_2 and Pd_{NPs}/f-G hybrids (Fig. 4, panel C and Fig. S5,† panel C, respectively). Markedly, the recorded ring current corresponds to the amount of the hydrogen peroxide intermediate produced at the disk electrode during the ORR, providing us not only a more accurate way to calculate the n value, but also a reliable method to estimate the percentage (%) of the produced H_2O_2.[45] In this regard, the electron transfer number and the H_2O_2 yield for Pd_{NPs}/f-MoS_2 in the potential range from 0.2 to 0.5 V (*vs.* Hg/HgO) were found to be 3.6 and 20%, respectively, suggesting that the oxygen reduction was mostly proceeded through the four electron transfer route and the main product was water. In general, the four-electron pathway is considered as more efficient and it is highly preferred in energy conversion applications. On the other hand, in the case of Pd_{NPs}/f-G, the two-electron and four-electron pathways coexist as n and % H_2O_2 were calculated to be 3.1 and 47%, respectively. Markedly, these results are consistent with those extracted through the K–L method.

Next, to gain insight into the rate-determining step involved in the oxygen electroreduction, the mass transfer corrected Tafel plots for all tested catalysts were constructed. As shown in Fig. 5, in the low current density region (region I), the Pd_{NPs}/f-MoS_2 and Pd_{NPs}/f-G hybrids exhibited a slope of −40 and −70 mV dec^{-1}, respectively, which are roughly close to that of Pd/C (−46 mV dec^{-1}). Actually, a Tafel slope near −60 mV dec^{-1} in this region indicates that the reaction rate is governed by the surface oxide coverage (Temkin adsorption mechanism).[46] In the high current density region (region II), a Tafel slope value of −180 mV dec^{-1} was recorded for both Pd_{NPs}/f-MoS_2 and Pd_{NPs}/f-G, whereas the corresponding value for the commercial catalyst was found to be −112 mV dec^{-1}. The higher Tafel value in region II is ascribed to a switch in the oxygen reduction mechanism since at these potentials the significant oxide coverage ceases to exist. In more depth, a slope close to −120 mV dec^{-1} indicates that the ORR is limited by the transfer of the first electron to the oxygen molecule (Langmuir adsorption), while for a value around −200 mV dec^{-1}, the adsorption of molecular oxygen has been proposed as the rate-determining step.[47,48] Therefore, the abovementioned results suggest a different rate-determining step in region II for the hybrid materials and the benchmark Pd/C catalyst.

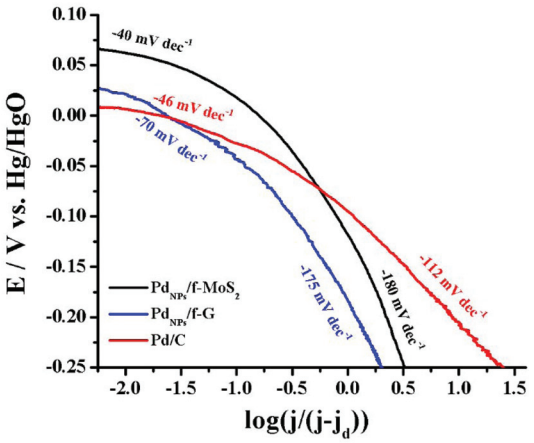

Fig. 5 Tafel plot for the Pd_{NPs}/f-MoS_2 and Pd_{NPs}/f-G hybrid electrocatalyst as compared to those due to Pd/C. Data derived from Fig. 3A.

Table 1 summarizes the electrochemical performance towards the ORR for all tested materials. Overall, it can be deduced that Pd_{NPs} immobilized onto MoS_2 sheets covalently functionalized with free amino groups (Pd_{NPs}/f-MoS_2) manifested improved electrocatalytic activity and stability as compared with those supported on graphene layers bearing analogous functionalities (Pd_{NPs}/f-G). Therefore, these results indicate that TMD nanosheets can be used as an alternative to graphene substrates for the development of novel and highly active hybrid electrocatalysts. Interestingly, the superior performance of the MoS_2 based hybrid over Pd_{NPs}/f-G is attributed to the following reasons. First, the covalent functionalization of graphene induces interruption of its continuous π-electron network through the introduction of sp^3 defect sites, thereby resulting in the degradation of its extraordinary electronic properties.[49] On the other hand, in the case of MoS_2, as mentioned before, the covalent attachment of the organic moieties takes place at the edges of the MoS_2 layers, keeping the basal plane intact and thus preserving its intrinsic properties.[24,50] At the same time, the high affinity of Pd_{NPs} with the free amino groups implies enhanced electronic interactions between them and the f-MoS_2 substrate, which are essential for the good ORR performance and long-term stability of the resulting hybrids. Here, it is worth noting that the high concentration of d electrons on the MoS_2 surface provides an additional mechanism for the nanoparticle stabilization, contributing to the remarkable durability of the Pd_{NPs}/MoS_2 catalyst.[51] Lastly, the surfactant-free synthesis of the hybrid material further improves its ORR activity by providing more active sites on the nanoparticle surface.[35,52]

An overview of the recently developed hybrid ORR electrocatalysts based on Pd_{NPs} and MoS_2 nanosheets is provided in Table S1.† For instance, Pd_{NPs} was formed and *in situ* immobilized on exfoliated MoS_2 *via* a sonochemical method.[26] The

Table 1 ORR electrochemical parameters for $Pd_{NPs}/f\text{-}MoS_2$ and $Pd_{NPs}/f\text{-}G$ as compared to those of Pd/C and $f\text{-}MoS_2$

Catalyst	Onset potential (mV *vs.* Hg/HgO)	Half-wave potential (mV *vs.* Hg/HgO)	Diffusion-limited current density[a] (mA cm^{-2})	Kinetic current density[b] (mA cm^{-2})	Tafel slopes	n_{K-L}	n_{RRDE}	H_2O_2 yield (%)
$Pd_{NPs}/f\text{-}MoS_2$	+66	−116	5.70	2.65	−40/−180	3.6–4.0	3.6	20
$Pd_{NPs}/f\text{-}MoS_2$[c]	+52	−120	5.20	2.40	—	—	—	—
$Pd_{NPs}/f\text{-}G$	+15	−168	3.90	0.58	−70/−175	3.4–3.6	3.1	47
$Pd_{NPs}/f\text{-}G$[c]	0	−194	3.00	0.35	—	—	—	—
$f\text{-}MoS_2$	−236	−360	1.47	0.00	—	2.1–2.3	—	—
Pd/C	+13	−93	5.40	2.00	−46/−112	3.8–4.0	3.8	<10
Pd/C[c]	−11	−135	3.70	0.69	—	—	—	—

[a] At 1600 rpm rotation rate (at ~0.50 V *vs.* Hg/HgO). [b] Calculated at −60 mV *vs.* Hg/HgO using the K–L equation. [c] After 10 000 s of the chronoamperometric experiment.

obtained Pd/MoS_2 hybrid exhibited an onset potential of −100 mV *vs.* SCE along with a diffusion-limited current density of 5.20 mA cm^{-2} in alkaline medium. Furthermore, the hybrid electrocatalyst outperformed the commercial one in terms of long-term stability. In a more recent work, a hybrid material based on palladium sulfide (PdS) nanoparticles supported on the MoS_2/N-doped graphene heterostructure (PdS–MoS_2/N-G) has been developed through a two-step thermolysis process while its ORR performance was examined under alkaline conditions.[27] Markedly, the hybrid catalyst demonstrated more positive onset and half-wave potential values (−146 and −214 mV *vs.* SCE, respectively) as well as a greater diffusion limited current density (4.1 mA cm^{-2}) than those of MoS_2/N-G and PdS/N-G references, despite failing to surpass the commercial Pt/C catalyst. Based on these data, the current $Pd_{NPs}/f\text{-}MoS_2$ hybrid is ranked among the top TMD-supported ORR electrocatalysts reported in the literature.

Experimental section

Materials

All chemicals and solvents were purchased from Aldrich and used without further purification unless otherwise stated.

Preparation of functionalized MoS_2 ($f\text{-}MoS_2$)

First, a chlorosulfonic acid assisted method was applied for MoS_2 exfoliation from the bulk in the form of semiconducting nanosheets.[8] Next, the covalent functionalization of MoS_2 sheets was achieved by employing 1,2-dithiolane units bearing an ethylene glycol alkyl chain terminated to a butoxycarbonyl (BOC)-protected amine.[24] In short, exfoliated MoS_2 (25 mg) and a 1,2-dithiolane derivative (30 mg) were dissolved in *N*,*N*-dimethylformamide (15 mL) and the reaction mixture was heated at 70 °C under stirring for 3 days. After this period, the mixture was filtered through a PTFE membrane filter (0.2 μm pore size) and the solid residue was extensively washed with dichloromethane. To cleave the BOC protecting group, the BOC modified MoS_2 nanosheets (20 mg) were redispersed in dichloromethane and treated with gaseous HCl. Finally, the reaction mixture was left under stirring overnight, filtered through a PTFE membrane (0.2 μm pore size), washed with dichloromethane and neutralized with triethylamine to yield the amino functionalized MoS_2 sheets ($f\text{-}MoS_2$).

Preparation of functionalized graphene (f-G)

Graphene oxide (GO) was prepared by following a modified Hummers' method.[53] Briefly, graphite powder was mixed with concentrated sulfuric acid, sodium nitrate and potassium permanganate to obtain a brownish slurry and the mixture was heated at 50 °C for 24 h. The suspension was diluted with water and hydrogen peroxide was added to get a higher oxidation degree. GO was finally obtained after washing with distilled water when the pH value became neutral. To prepare amino functionalized graphene (f-G), first, GO (20 mg) was activated by treatment with thionyl chloride (7 mL) at 66 °C overnight under an inert atmosphere. Next, the excess thionyl chloride was evaporated under reduced pressure and the remaining solid was carefully washed with dry tetrahydrofuran under nitrogen. The as-produced acyl-chlorinated graphene was dispersed in dry tetrahydrofuran (10 mL) followed by the addition of *N-tert*-butoxycarbonyl-2,2′-(ethylenedioxy)bis-ethylamine (300 mg) dissolved in dry tetrahydrofuran (5 mL). The reaction mixture was refluxed for 3 days. The resulting suspension was filtered over a PTFE membrane filter (0.2 μm pore size) and the filtrate was extensively washed with dichloromethane to remove organic residues before being dried under vacuum. Afterwards, the material was dispersed in dry dichloromethane and treated with gaseous HCl overnight to cleave the *N-tert*-butoxycarbonyl moieties. Finally, the reaction mixture was filtered through a PTFE membrane (0.2 μm pore size), washed with dichloromethane and neutralized with triethylamine to yield the amino functionalized graphene sheets (f-G).

Preparation of $Pd_{NPs}/f\text{-}MoS_2$ and $Pd_{NPs}/f\text{-}G$ hybrids

For a typical synthesis of $Pd_{NPs}/f\text{-}MoS_2$, $f\text{-}MoS_2$ (8 mg) was ultrasonically dispersed in ethylene glycol (20 mL) to form a black homogeneous dispersion. Subsequently, potassium tetrachloropallade (6 mg) dissolved in ethylene glycol (5 mL) was mixed with the as-prepared polyol solution, degassed, and stirred for 30 min. Then, sodium borohydride (3.5 mg) dissolved in ethylene glycol (3 mL) was added gradually, and the

reaction mixture was stirred under nitrogen for 60 min. The resulting suspension was washed with ethanol and vacuum dried. The same procedure was followed to prepare the Pd_{NPs}/f-G hybrid. In both Pd_{NPs}/f-MoS_2 and Pd_{NPs}/f-G hybrids, the designed Pd_{NPs} loading was 20 wt%.

Physical characterization

Scanning transmission electron microscopy (STEM) combined with EDS and electron energy-loss spectroscopy (EELS) were performed using a JEOL JEM-2100F microscope equipped with a couple of JEOL Centurio EDS detectors and a Gatan Quantum electron spectrometer at an electron accelerating voltage of 60 kV. An EELS chemical map of Pd was obtained by measuring its $M_{4,5}$ edge signals at each point of a scanned area. Infrared (IR) spectra were acquired on a Fourier transform IR spectrometer (Equinox 55 from Bruker Optics) equipped with a single reflection diamond ATR accessory (DuraSamp1IR II by SensIR Technologies). Raman measurements were performed with a Renishaw confocal spectrometer at 633 nm. Thermogravimetric analysis (TGA) was carried out using a TGA Q500 V20.2 Build 27 instrument by TA under a nitrogen inert atmosphere.

Catalyst preparation and deposition onto the working electrode

To prepare the catalyst ink, 4.0 mg of the hybrid catalytic powder were dispersed in a mixture of solvents (1 mL) containing water, isopropanol, and 5% Nafion (v/v/v = 4 : 1 : 0.02) and sonicated for 15 min. The working electrode was first cleaned through polishing using 6, 3 and 1 mm diamond pastes, rinsed with deionized water, and sonicated in double-distilled water. Then, 8.5 μL aliquots of the catalyst ink were cast on the electrode surface and dried at room temperature.

Electrochemical testing and calculations

All the electrochemical measurements were carried out using an Autolab PGSTAT128 N potentiostat/galvanostat equipped with a dual mode bipotentiostat (BA module). The working electrode (Autolab RRDE electrode tips) consisted of a Teflon-embedded glassy carbon (GC) disk/Pt ring rotating assembly (5 mm electrode disk diameter, 375 μm electrode gap, collection efficiency N = 0.249). As the counter electrode, a platinum wire was used and as the reference electrode an Hg/HgO (0.1 M KOH) electrode was placed into the Luggin capillary. The ORR measurements were realized at room temperature in O_2-saturated aqueous 0.1 M KOH electrolyte. Linear sweep voltammetry (LSV) measurements on the disk electrode were conducted from −0.8 to +0.2 V *vs.* Hg/HgO at different rotation rates with a scan rate of 5 mV s^{-1}. At the ring, the potential was fixed at +1.0 V *vs.* Hg/HgO and the current response was recorded. Chronoamperometric measurements for all materials were probed at −0.40 V *vs.* Hg/HgO at a rotation rate of 1600 rpm for 10 000 s.

The kinetic current densities (j_k) were calculated using the Koutecký–Levich (K–L) equation:

$$1/j = 1/j_d + 1/j_k \quad (1)$$

where j and j_d are the experimentally measured and the diffusion-limited current density, respectively. The number of electrons transferred in the reduction of one O_2 molecule (n) can be determined by modifying the K–L equation as follows:

$$1/j = 1/j_d + 1/j_k = 1/B\omega^{1/2} + 1/j_k \quad (2)$$

where ω is the angular velocity and B is the K–L slope given by the following equation:

$$B = 0.20nFC_0D_0^{2/3}\nu^{1/6}. \quad (3)$$

Here, n is the electron transfer number, F is the Faraday constant (F = 96 485 C mol^{-1}), D_0 is the diffusion coefficient of O_2 ($D_0 = 1.9 \times 10^{-5}$ cm^2 s^{-1}), ν is the kinematic viscosity of the solution (ν = 0.01 cm^2 s^{-1}), and C_0 is the concentration of dissolved O_2 in the solution ($C_0 = 1.2 \times 10^{-6}$ mol cm^{-3}). The constant of 0.2 is adopted when the rotation speed is expressed in revolutions per minute (rpm). Tafel plots (potential *vs.* log[j/(j_d − j)]) were calculated in the mixed kinetic–diffusion region at a single electrode rotation rate (ω = 1600 rpm).

Based on the RRDE data, the n value and the percentage (%) of the produced H_2O_2 can be determined using the following equations:

$$n = 4I_{Disk}/(I_{Disk} + I_{Ring}/N) \quad (4)$$

$$\%H_2O_2 = (200\ I_{Ring}/N)/(I_{Disk} + I_{Ring}/N) \quad (5)$$

where I_{disk} is the current of the disk electrode, I_{ring} is the current of the ring electrode, and N is the collection efficiency of the Pt ring, which was provided as 0.249 by the manufacturer.

The capacitance values were calculated from the CV curves obtained in N_2-saturated aqueous 0.1 M KOH according to eqn (6):

$$C = \int I\mathrm{d}V/\Delta V \times \nu \quad (6)$$

where C (F) is the specific capacitance; $\int I\mathrm{d}V(C)$ is the integrated area of the CV curve; ΔV (V) is the potential window and v is the scan rate (V s^{-1}).

Conclusions

In summary, the fabrication of a novel hybrid ORR electrocatalyst based on covalently functionalized MoS_2 nanosheets bearing free amino moieties and Pd nanoparticles, Pd_{NPs}/f-MoS_2, through a simple procedure was accomplished. For comparison, an analogous catalyst based on modified graphene, Pd_{NPs}/f-G, was also obtained. Complementary spectroscopic techniques and thermogravimetric analysis confirmed and quantified the covalent attachment of the organic functionalities onto MoS_2 and graphene. TEM imaging along with EDS/EELS elemental analysis revealed the immobilization of 2–3 nm Pd_{NPs} onto both 2D substrates, while the presence of agglomeration was not observed. The preservation of the MoS_2 intrinsic properties during the functionalization process allowed us, in contrast to graphene, to fully exploit the benefits

of the covalent modification, leading to improved electrocatalytic activities and stability toward the ORR in an alkaline medium for the Pd_{NPs}/f-MoS_2 hybrid, outperforming not only its graphene based counterpart, but also the benchmark Pd/C catalyst. In more detail, the onset potential value for Pd_{NPs}/f-MoS_2 was found to be approximately 50 mV more positive than that of Pd_{NPs}/f-G and Pd/C, whereas, with a kinetic current density value of 2.65 mA cm^{-2}, the MoS_2 based electrocatalyst possesses a 4.5-fold and by 46% greater activity over that registered for the graphene based catalyst and the commercial catalyst, respectively. Furthermore, Pd_{NPs}/f-MoS_2 proved to be remarkably stable, exhibiting the lowest activity loss (~16%) after 10 000 s, among the tested electrocatalysts. A detailed analysis of the reaction kinetics suggested that the reduction of oxygen on the Pd_{NPs}/f-MoS_2 hybrid abided mainly by the direct four-electron route, with a low H_2O_2 yield. All in all, these findings pave the way for future designs of high-performance TMD-based ORR electrocatalysts.

Conflicts of interest

There are no conflicts to declare.

Acknowledgements

This research is co-financed by Greece and the European Union (European Social Fund- ESF) through the Operational Programme "Human Resources Development, Education and Lifelong Learning" in the context of the project "Reinforcement of Postdoctoral Researchers - 2nd Cycle" (MIS-5033021), implemented by the State Scholarships Foundation (IKY). Y. S. and K. S. acknowledge JSPS KAKENHI (Grant No. JP19K05223 and JP16H06333, respectively) for financial support.

Notes and references

1 X. Tian, X. F. Lu, B. Y. Xia and X. W. Lou, *Joule*, 2020, **4**, 45–68.
2 H. Li, C. Chen, D. Yan, Y. Wang, R. Chen, Y. Zou and S. Wang, *J. Mater. Chem. A*, 2019, **7**, 23432–23450.
3 D. K. Perivoliotis and N. Tagmatarchis, *Carbon*, 2017, **118**, 493–510.
4 S. Jayabal, G. Saranya, J. Wu, Y. Liu, D. Geng and X. Meng, *J. Mater. Chem. A*, 2017, **5**, 24540–24563.
5 O. My Na, N. T. Xuan Huynh, P. T. Thi, V. Chihaia and D. Ngoc Son, *RSC Adv.*, 2020, **10**, 8460–8469.
6 A. K. Geim and I. V. Grigorieva, *Nature*, 2013, **499**, 419–425.
7 X. Li and H. Zhu, *J. Materiomics*, 2015, **1**, 33–44.
8 G. Pagona, C. Bittencourt, R. Arenal and N. Tagmatarchis, *Chem. Commun.*, 2015, **51**, 12950–12953.
9 X. Fan, P. Xu, Y. C. Li, D. Zhou, Y. Sun, M. A. T. Nguyen, M. Terrones and T. E. Mallouk, *J. Am. Chem. Soc.*, 2016, **138**, 5143–5149.
10 Z. Lei, J. Zhan, L. Tang, Y. Zhang and Y. Wang, *Adv. Energy Mater.*, 2018, **8**, 1703482.
11 S. Shi, Z. Sun and Y. H. Hu, *J. Mater. Chem. A*, 2018, **6**, 23932–23977.
12 K. F. Mak, C. Lee, J. Hone, J. Shan and T. F. Heinz, *Phys. Rev. Lett.*, 2010, **105**, 136805.
13 G. Eda, H. Yamaguchi, D. Voiry, T. Fujita, M. Chen and M. Chhowalla, *Nano Lett.*, 2011, **11**, 5111–5116.
14 C. Zhu, D. Gao, J. Ding, D. Chao and J. Wang, *Chem. Soc. Rev.*, 2018, **47**, 4332–4356.
15 Z. Li, X. Meng and Z. Zhang, *J. Photochem. Photobiol., C*, 2018, **35**, 39–55.
16 K. Wang, L. Li, Y. Liu, C. Zhang and T. Liu, *Adv. Mater. Interfaces*, 2016, **3**, 1600665.
17 Y. Wang, K. Wang, C. Zhang, J. Zhu, J. Xu and T. Liu, *Small*, 2019, **15**, 1903816.
18 K. Wang, J. Yang, J. Zhu, L. Li, Y. Liu, C. Zhang and T. Liu, *J. Mater. Chem. A*, 2017, **5**, 11236–11245.
19 J. Yang, J. Zhu, J. Xu, C. Zhang and T. Liu, *ACS Appl. Mater. Interfaces*, 2017, **9**, 44550–44559.
20 X. Chen and A. R. McDonald, *Adv. Mater.*, 2016, **28**, 5738–5746.
21 A. Stergiou and N. Tagmatarchis, *Chem. – Eur. J.*, 2018, **24**, 18246–18257.
22 P. Vishnoi, A. Sampath, U. V. Waghmare and C. N. R. Rao, *Chem. – Eur. J.*, 2017, **23**, 886–895.
23 X. Chen, N. C. Berner, C. Backes, G. S. Duesberg and A. R. McDonald, *Angew. Chem., Int. Ed.*, 2016, **55**, 5803–5808.
24 R. Canton-Vitoria, Y. Sayed-Ahmad-Baraza, M. Pelaez-Fernandez, R. Arenal, C. Bittencourt, C. P. Ewels and N. Tagmatarchis, *npj 2D Mater. Appl.*, 2017, **1**, 13.
25 E. Lee and Y.-U. Kwon, *RSC Adv.*, 2016, **6**, 47468–47473.
26 L.-X. Zuo, L.-P. Jiang and J.-J. Zhu, *Ultrason. Sonochem.*, 2017, **35**, 681–688.
27 L. G. Bach, M. L. N. Thi, Q. B. Bui and H. T. Nhac-Vu, *Synth. Met.*, 2019, **254**, 172–179.
28 S. Su, W. Cao, C. Zhang, X. Han, H. Yu, D. Zhu, J. Chao, C. Fan and L. Wang, *RSC Adv.*, 2016, **6**, 76614–76620.
29 M. Liu, R. Zhang and W. Chen, *Chem. Rev.*, 2014, **114**, 5117–5160.
30 D. Perivoliotis, Y. Sato, K. Suenaga and N. Tagmatarchis, *Chem. – Eur. J.*, 2019, **25**, 11105–11113.
31 D. K. Perivoliotis, Y. Sato, K. Suenaga and N. Tagmatarchis, *ACS Appl. Energy Mater.*, 2018, **1**, 3869–3880.
32 M. A. Koklioti, T. Skaltsas, Y. Sato, K. Suenaga, A. Stergiou and N. Tagmatarchis, *Nanoscale*, 2017, **9**, 9685–9692.
33 S. Park, D. A. Dikin, S. T. Nguyen and R. S. Ruoff, *J. Phys. Chem. C*, 2009, **113**, 15801–15804.
34 J. Liu, J. Hao, C. Hu, B. He, J. Xi, J. Xiao, S. Wang and Z. Bai, *J. Phys. Chem. C*, 2018, **122**, 2696–2703.
35 D. Alba-Molina, A. R. Puente Santiago, J. J. Giner-Casares, E. Rodríguez-Castellón, M. T. Martín-Romero, L. Camacho, R. Luque and M. Cano, *J. Mater. Chem. A*, 2019, **7**, 20425–20434.

36 H. Li, Q. Zhang, C. C. R. Yap, B. K. Tay, T. H. T. Edwin, A. Olivier and D. Baillargeat, *Adv. Funct. Mater.*, 2012, **22**, 1385–1390.
37 S. Bae, N. Sugiyama, T. Matsuo, H. Raebiger, K.-I. Shudo and K. Ohno, *Phys. Rev. Appl.*, 2017, **7**, 024001.
38 K. C. Knirsch, N. C. Berner, H. C. Nerl, C. S. Cucinotta, Z. Gholamvand, N. McEvoy, Z. Wang, I. Abramovic, P. Vecera, M. Halik, S. Sanvito, G. S. Duesberg, V. Nicolosi, F. Hauke, A. Hirsch, J. N. Coleman and C. Backes, *ACS Nano*, 2015, **9**, 6018–6030.
39 X. Chen, P. Denninger, T. Stimpel-Lindner, E. Spiecker, G. S. Duesberg, C. Backes, K. C. Knirsch and A. Hirsch, *Chem. – Eur. J.*, 2020, **26**, 6535–6544.
40 R. Canton-Vitoria, H. B. Gobeze, V. M. Blas-Ferrando, J. Ortiz, Y. Jang, F. Fernández-Lázaro, Á. Sastre-Santos, Y. Nakanishi, H. Shinohara, F. D'Souza and N. Tagmatarchis, *Angew. Chem., Int. Ed.*, 2019, **58**, 5712–5717.
41 J.-B. Wu, M.-L. Lin, X. Cong, H.-N. Liu and P.-H. Tan, *Chem. Soc. Rev.*, 2018, **47**, 1822–1873.
42 M. Lukaszewski, M. Soszko and A. Czerwiński, *Int. J. Electrochem. Sci.*, 2016, **11**, 4442–4469.
43 J. Benson, Q. Xu, P. Wang, Y. Shen, L. Sun, T. Wang, M. Li and P. Papakonstantinou, *ACS Appl. Mater. Interfaces*, 2014, **6**, 19726–19736.
44 A. Stergiou, D. K. Perivoliotis and N. Tagmatarchis, *Nanoscale*, 2019, **11**, 7335–7346.
45 R. Zhou, Y. Zheng, M. Jaroniec and S.-Z. Qiao, *ACS Catal.*, 2016, **6**, 4720–4728.
46 N. P. Subramanian, T. Greszler, J. Zhang, W. Gu and R. R. Makharia, *ECS Trans.*, 2011, **41**, 985–1007.
47 Q. He, Q. Li, S. Khene, X. Ren, F. E. López-Suárez, D. Lozano-Castelló, A. Bueno-López and G. Wu, *J. Phys. Chem. C*, 2013, **117**, 8697–8707.
48 C. Lee, S. Ozden, C. S. Tewari, O.-K. Park, R. Vajtai, K. Chatterjee and P. M. Ajayan, *ChemSusChem*, 2018, **11**, 2960–2966.
49 Z. Zhang, H. Huang, X. Yang and L. Zang, *J. Phys. Chem. Lett.*, 2011, **2**, 2897–2905.
50 L. Guardia, J. I. Paredes, J. M. Munuera, S. Villar-Rodil, M. Ayán-Varela, A. Martínez-Alonso and J. M. D. Tascón, *ACS Appl. Mater. Interfaces*, 2014, **6**, 21702–21710.
51 Y. Wang, B. Wang, R. Huang, B. Gao, F. Kong and Q. Zhang, *Phys. E*, 2014, **63**, 276–282.
52 X. Zhang, J. Zhu, C. S. Tiwary, Z. Ma, H. Huang, J. Zhang, Z. Lu, W. Huang and Y. Wu, *ACS Appl. Mater. Interfaces*, 2016, **8**, 10858–10865.
53 W. S. Hummers and R. E. Offeman, *J. Am. Chem. Soc.*, 1958, **80**, 1339–1339.